FERMILAB-PUB-23-410-ND

First demonstration for a LArTPC-based search for intranuclear neutron-antineutron transitions and annihilation in ^{40}Ar using the MicroBooNE detector

P. Abratenko,[36] O. Alterkait,[36] D. Andrade Aldana,[15] L. Arellano,[20] J. Asaadi,[35] A. Ashkenazi,[33] S. Balasubramanian,[12] B. Baller,[12] G. Barr,[26] D. Barrow,[26] J. Barrow,[21,33] V. Basque,[12] O. Benevides Rodrigues,[15] S. Berkman,[12] A. Bhanderi,[20] A. Bhat,[7] M. Bhattacharya,[12] M. Bishai,[3] A. Blake,[17] B. Bogart,[22] T. Bolton,[16] J. Y. Book,[14] L. Camilleri,[10] Y. Cao,[20] D. Caratelli,[4] I. Caro Terrazas,[9] F. Cavanna,[12] G. Cerati,[12] Y. Chen,[29] J. M. Conrad,[21] M. Convery,[29] L. Cooper-Troendle,[27,40] J. I. Crespo-Anadón,[6] R. Cross,[39] M. Del Tutto,[12] S. R. Dennis,[5] P. Detje,[5] A. Devitt,[17] R. Diurba,[2] Z. Djurcic,[1] R. Dorrill,[15] K. Duffy,[26] S. Dytman,[27] B. Eberly,[31] P. Englezos,[28] A. Ereditato,[7,12] J. J. Evans,[20] R. Fine,[18] O. G. Finnerud,[20] W. Foreman,[15] B. T. Fleming,[7] N. Foppiani,[14] D. Franco,[7] A. P. Furmanski,[23] D. Garcia-Gamez,[13] S. Gardiner,[12] G. Ge,[10] S. Gollapinni,[18,34] O. Goodwin,[20] E. Gramellini,[12] P. Green,[26] H. Greenlee,[12] W. Gu,[3] R. Guenette,[20] P. Guzowski,[20] L. Hagaman,[7] O. Hen,[21] R. Hicks,[18] C. Hilgenberg,[23] G. A. Horton-Smith,[16] Z. Imani,[36] B. Irwin,[23] R. Itay,[29] C. James,[12] X. Ji,[24,3] L. Jiang,[38] J. H. Jo,[3] R. A. Johnson,[8] Y.-J. Jwa,[10] D. Kalra,[10] N. Kamp,[21] G. Karagiorgi,[10] W. Ketchum,[12] M. Kirby,[12] T. Kobilarcik,[12] I. Kreslo,[2] M. B. Leibovitch,[4] I. Lepetic,[28] J.-Y. Li,[11] K. Li,[40] Y. Li,[3] K. Lin,[28] B. R. Littlejohn,[15] H. Liu,[3] W. C. Louis,[18] X. Luo,[4] C. Mariani,[38] D. Marsden,[20] J. Marshall,[39] N. Martinez,[16] D. A. Martinez Caicedo,[30] S. Martynenko,[3] A. Mastbaum,[28] N. McConkey,[37] V. Meddage,[16] J. Micallef,[21,36] K. Miller,[7] A. Mogan,[9] T. Mohayai,[12] M. Mooney,[9] A. F. Moor,[5] C. D. Moore,[12] L. Mora Lepin,[20] M. M. Moudgalya,[20] S. Mulleriababu,[2] D. Naples,[27] A. Navrer-Agasson,[20] N. Nayak,[3] M. Nebot-Guinot,[11] J. Nowak,[17] N. Oza,[10] O. Palamara,[12] N. Pallat,[23] V. Paolone,[27] A. Papadopoulou,[1] V. Papavassiliou,[25] H. B. Parkinson,[11] S. F. Pate,[25] N. Patel,[17] Z. Pavlovic,[12] E. Piasetzky,[33] I. D. Ponce-Pinto,[40] I. Pophale,[17] X. Qian,[3] J. L. Raaf,[12] V. Radeka,[3] A. Rafique,[1] M. Reggiani-Guzzo,[20] L. Ren,[25] L. Rochester,[29] J. Rodriguez Rondon,[30] M. Rosenberg,[36] M. Ross-Lonergan,[18] C. Rudolf von Rohr,[2] I. Safa,[10] G. Scanavini,[40] D. W. Schmitz,[7] A. Schukraft,[12] W. Seligman,[10] M. H. Shaevitz,[10] R. Sharankova,[12] J. Shi,[5] E. L. Snider,[12] M. Soderberg,[32] S. Söldner-Rembold,[20] J. Spitz,[22] M. Stancari,[12] J. St. John,[12] T. Strauss,[12] A. M. Szelc,[11] W. Tang,[34] N. Taniuchi,[5] K. Terao,[29] C. Thorpe,[17,20] D. Torbunov,[3] D. Totani,[4] M. Toups,[12] Y.-T. Tsai,[29] J. Tyler,[16] M. A. Uchida,[5] T. Usher,[29] B. Viren,[3] M. Weber,[2] H. Wei,[19] A. J. White,[7] S. Wolbers,[12] T. Wongjirad,[36] M. Wospakrik,[12] K. Wresilo,[5] N. Wright,[21] W. Wu,[12,27] E. Yandel,[4] T. Yang,[12] L. E. Yates,[12] H. W. Yu,[3] G. P. Zeller,[12] J. Zennamo,[12] and C. Zhang[3]

(The MicroBooNE Collaboration)*

[1] *Argonne National Laboratory (ANL), Lemont, IL, 60439, USA*
[2] *Universität Bern, Bern CH-3012, Switzerland*
[3] *Brookhaven National Laboratory (BNL), Upton, NY, 11973, USA*
[4] *University of California, Santa Barbara, CA, 93106, USA*
[5] *University of Cambridge, Cambridge CB3 0HE, United Kingdom*
[6] *Centro de Investigaciones Energéticas, Medioambientales y Tecnológicas (CIEMAT), Madrid E-28040, Spain*
[7] *University of Chicago, Chicago, IL, 60637, USA*
[8] *University of Cincinnati, Cincinnati, OH, 45221, USA*
[9] *Colorado State University, Fort Collins, CO, 80523, USA*
[10] *Columbia University, New York, NY, 10027, USA*
[11] *University of Edinburgh, Edinburgh EH9 3FD, United Kingdom*
[12] *Fermi National Accelerator Laboratory (FNAL), Batavia, IL 60510, USA*
[13] *Universidad de Granada, Granada E-18071, Spain*
[14] *Harvard University, Cambridge, MA 02138, USA*
[15] *Illinois Institute of Technology (IIT), Chicago, IL 60616, USA*
[16] *Kansas State University (KSU), Manhattan, KS, 66506, USA*
[17] *Lancaster University, Lancaster LA1 4YW, United Kingdom*
[18] *Los Alamos National Laboratory (LANL), Los Alamos, NM, 87545, USA*
[19] *Louisiana State University, Baton Rouge, LA, 70803, USA*
[20] *The University of Manchester, Manchester M13 9PL, United Kingdom*
[21] *Massachusetts Institute of Technology (MIT), Cambridge, MA, 02139, USA*
[22] *University of Michigan, Ann Arbor, MI, 48109, USA*
[23] *University of Minnesota, Minneapolis, MN, 55455, USA*
[24] *Nankai University, Nankai District, Tianjin 300071, China*
[25] *New Mexico State University (NMSU), Las Cruces, NM, 88003, USA*
[26] *University of Oxford, Oxford OX1 3RH, United Kingdom*
[27] *University of Pittsburgh, Pittsburgh, PA, 15260, USA*
[28] *Rutgers University, Piscataway, NJ, 08854, USA*

arXiv:2308.03924v2 [hep-ex] 9 Aug 2023

[29] SLAC National Accelerator Laboratory, Menlo Park, CA, 94025, USA
[30] South Dakota School of Mines and Technology (SDSMT), Rapid City, SD, 57701, USA
[31] University of Southern Maine, Portland, ME, 04104, USA
[32] Syracuse University, Syracuse, NY, 13244, USA
[33] Tel Aviv University, Tel Aviv, Israel, 69978
[34] University of Tennessee, Knoxville, TN, 37996, USA
[35] University of Texas, Arlington, TX, 76019, USA
[36] Tufts University, Medford, MA, 02155, USA
[37] University College London, London WC1E 6BT, United Kingdom
[38] Center for Neutrino Physics, Virginia Tech, Blacksburg, VA, 24061, USA
[39] University of Warwick, Coventry CV4 7AL, United Kingdom
[40] Wright Laboratory, Department of Physics, Yale University, New Haven, CT, 06520, USA

(Dated: August 10, 2023)

Dedicated to the memory of William J. Willis.

In this paper, we present a novel methodology to search for intranuclear neutron-antineutron transition ($n \rightarrow \bar{n}$) followed by annihilation within an ^{40}Ar nucleus, using the MicroBooNE liquid argon time projection chamber (LArTPC) detector. A discovery of $n \rightarrow \bar{n}$ transition or increased lower limit on the lifetime of this process would either constitute physics beyond the Standard Model or greatly constrain theories of baryogenesis, respectively. The approach presented in this paper makes use of deep learning methods to select $n \rightarrow \bar{n}$ events based on their unique features and differentiate them from cosmogenic backgrounds. The achieved signal and background efficiencies are (70±6)% and (0.0020±0.0003)%, respectively. A demonstration of a search is performed with a data set corresponding to an exposure of 3.32×10^{26} neutron-years, and where the background rate is constrained through direct measurement, assuming the presence of a negligible signal. With this approach, no excess of events over the background prediction is observed, setting a demonstrative lower bound on the $n \rightarrow \bar{n}$ lifetime in ^{40}Ar of $\tau_{\mathrm{m}} > 1.1 \times 10^{26}$ years, and on the free $n \rightarrow \bar{n}$ transition time of $\tau_{\mathrm{n}-\bar{\mathrm{n}}} > 2.6 \times 10^{5}$ s, each at the 90% confidence level. This analysis represents a first-ever proof-of-principle demonstration of the ability to search for this rare process in LArTPCs with high efficiency and low background.

I. INTRODUCTION

Processes such as neutron-antineutron transition [1] can provide a unique test of theoretical extensions to the Standard Model of particle physics that allow for the violation of baryon number conservation [2]. The transition of a neutron to antineutron ($n \rightarrow \bar{n}$) is a theoretically motivated beyond-Standard Model process that violates baryon number by two units [1, 3]. The process of intranuclear $n \rightarrow \bar{n}$ involves the transformation of a bound neutron into an antineutron. This antineutron then annihilates with a nearby nucleon (neutron or proton) and produces, on average, 3–4 final state pions [4, 5]. The branching ratios of $\bar{n}p$ and $\bar{n}n$ annihilation products are based on past measurements of $\bar{p}n$ and $\bar{p}p$ interactions, respectively [4–7]. In a vacuum, the final state pions produced by a motionless and unbound annihilating pair are expected to have zero total momentum and a total invariant mass corresponding to the sum of the masses of the two (anti)nucleons. Deviations from this expectation are due to nuclear effects—specifically, intranuclear Fermi motion of the annihilating (anti)nucleons, their nuclear binding energy, and final state interactions as the initial state mesons traverse the nuclear medium—leading to smearing effects of the observed final state kinematics. The annihilation has a star-like, spherical topological signature, which can be used to differentiate it from background interactions.

An experimental discovery or stringent lower bound, surpassing the current best limits [4, 8], on the rate of intranuclear $n \rightarrow \bar{n}$ would make an important contribution to our understanding of the baryon asymmetry of the Universe. To date, limits have been placed on the mean lifetime of this process by various experiments using either free neutrons or neutrons bound in nuclei [9–18]. The free-neutron $n \rightarrow \bar{n}$ lifetime ($\tau_{\mathrm{n}-\bar{\mathrm{n}}}$) and bound-neutron $n \rightarrow \bar{n}$ lifetime (τ_{m}) are related through a factor (R) [19, 20] as shown in Eq.(1), which accounts for the high suppression of the transition due to differences in the nuclear potentials of neutrons and antineutrons within the nucleus where this process could take place,

$$\tau_{\mathrm{m}} = R\tau^{2}_{\mathrm{n}-\bar{\mathrm{n}}}. \tag{1}$$

For ^{40}Ar nuclei, R is expected to take on a value of $5.6\times10^{22}\,\mathrm{s}^{-1}$ with an uncertainty of 20% [19]. The most stringent limit on the free neutron transition time is provided by ILL in Grenoble [8] at 0.86×10^{8} s at the 90% confidence level (CL), while the Super-Kamiokande experiment, using oxygen-bound neutrons and an associated suppression factor of $5.17 \times 10^{22}\,\mathrm{s}^{-1}$ [20, 21], corresponds to $\tau_{\mathrm{n}-\bar{\mathrm{n}}} > 4.7 \times 10^{8}$ s at the 90% CL [4].

This work presents a deep learning (DL)-based analysis of MicroBooNE data, making use of a sparse convolutional neural network (CNN) [22, 23], to search for $n \rightarrow \bar{n}$ like signals using primarily their topological signature. This analysis can be extended to future, larger liquid argon time projection chamber (LArTPC) detectors such as the Deep Underground Neutrino Experiment (DUNE) [24–26], which will enable a higher sensitivity to this rare process because of its much larger detector

* microboone_info@fnal.gov

mass. The results reported in this paper use the MicroBooNE off-beam data (data collected when the neutrino beam was not running) with a total exposure of 372 s, corresponding to 3.32×10^{26} neutron-years.

II. EXPERIMENTAL SETUP

The MicroBooNE LArTPC detector [27] employs an active volume of 85 metric tonnes of liquid argon (LAr). The detector is a 10.4 m long, 2.6 m wide, and 2.3 m high LArTPC and is located on-surface and on-axis to the Booster Neutrino Beamline [28] at Fermilab. Due to its on-surface location, the MicroBooNE detector is exposed to a large flux of cosmic rays, leading to a variety of cosmogenic activity in the detector. Charged particles produced from interactions within the LAr leave a trail of ionization electrons which drift, under the effect of a uniform electric field, with a maximum electron drift time of 2.3 ms towards anode wire planes. Three anode wire planes named U, V, and Y, with U and V plane wires oriented at $\pm 60^{\circ}$ relative to vertical, and Y plane wires oriented vertically, sense and collect the ionization charge. A light detection system composed of photomultiplier tubes (PMT) detects scintillation light produced in the interaction which in turn helps to determine the drift time (time taken by ionization electrons to drift to the anode wires), achieving 3D particle reconstruction. Data was collected from 2015–2021 and includes off-beam data during periods when there was no neutrino beam.

III. ANALYSIS OVERVIEW

The methodology used to search for intranuclear $n \to \bar{n}$ transition in MicroBooNE was developed using off-beam data that were recorded using an external, random trigger. Each trigger corresponds to an exposure of 2.3 ms (an "event"), the standard readout length of MicroBooNE. The readout window (or exposure interval) ensures that all ionization information associated with a given interaction at trigger time occuring anywhere in the active volume is collected by the readout. During this period, light and unbiased (raw) ionization charge data were collected and analyzed, searching for interaction "clusters" with a characteristic star-like topology. The dominant source of interactions during these short beam-off exposures come from cosmic ray muons (straight track-like features) and other cosmogenic activity, and/or products of their electromagnetic and hadronic showers, which are expected to contribute as the dominant background to the $n \to \bar{n}$ search. This source of background is unique to a search using the MicroBooNE detector, due to its on-surface location, whereas searches with detectors located deep underground, such as DUNE, are expected to be limited by atmospheric neutrino backgrounds.

Relevant to the analysis strategy, MicroBooNE does not use a dedicated Monte Carlo simulation for cosmic backgrounds but instead relies on *in-situ* measurements to directly measure and thus constrain the rate of these interactions. As such, a data-driven approach was followed to search for $n \to \bar{n}$ under the assumption of negligible signal being present in the data. In this approach, the off-beam data sample was divided into four statistically independent sub-samples, where 40% was reserved for analysis development and, in particular, to train machine learning algorithms, 50% was reserved as the test sample to determine signal selection efficiency and predict background rates, 5% was set aside for the development validation of a blinded analysis using "fake data", and the remaining 5% corresponding to 372 s of exposure was reserved as the "data" sample for the final measurement and reported results. This analysis was performed blind, with final data distributions and extracted $n \to \bar{n}$ limits obtained only *after* the review of the analysis. The data-driven approach used to generate the signal and background samples automatically enables accurate "modeling" of cosmogenic activity and noise sources, including any time dependence in the detector response. However, this approach assumes that there are no significant signal events in the off-beam data. This is a safe assumption, given the current best limits on $n \to \bar{n}$ from the Super-K experiment [4].

Signal $n \to \bar{n}$ interactions are simulated uniformly across the detector's active volume using the GENIE neutrino event generator (GENIE v.3.00.04) [29–31], where the (anti)nucleon's Fermi motion and binding energy are modeled using a local Fermi gas model, and the empirical, data-driven hA Intranuke algorithm is used to simulate final state interactions (FSI). The ^{40}Ar nucleus is assumed to be at rest during the $n \to \bar{n}$ process. The position of a neutron (to be oscillated into an antineutron) within the nucleus is simulated using GENIE's density profile of nucleons (Woods-Saxon distribution [32]),

$$\rho(r) = \frac{\rho_0}{1 + e^{\frac{r - R_0}{a}}} , \tag{2}$$

where r is the radial position inside the nucleus, $R_0 = r_0 A^{\frac{1}{3}}$ is the nuclear radius, with r_0 defined as 1.4 fm in GENIE. ρ_0 is normalized in order to express nuclear density as a probability distribution, and a is a parameter describing the surface thickness of the nucleus, set to $a = 0.54$ fm.

This analysis considers the annihilation of an antineutron with either a neutron or a proton and simulates the resulting products of annihilation (3–4 pions on an average) using the branching ratios informed by previous measurements [4–7], reproduced in Table I, accounting for the available kinematic phase-space on an event-by-event basis [31]. The final state particles are subsequently propagated through the detector with Geant4 [33]. This is followed by the custom detector simulation for the MicroBooNE detector [34–36] to take account of the detector response. The resulting simulated detector signals are overlaid with real data with cosmogenic activity.

TABLE I. Effective branching ratios for antineutron annihilation in ^{40}Ar, as implemented in GENIE. The branching ratios are adapted from analysis by the Super-K collaboration [4] and are derived from past antiproton annihilation measurements on hydrogen and deuterium, with a phase-space approximation [31].

$\bar{n}+p$		$\bar{n}+n$	
Channel	Branching ratio	Channel	Branching ratio
$\pi^+\pi^0$	1.2%	$\pi^+\pi^-$	2.0%
$\pi^+2\pi^0$	9.5%	$2\pi^0$	1.5%
$\pi^+3\pi^0$	11.9%	$\pi^+\pi^-\pi^0$	6.5%
$2\pi^+\pi^-\pi^0$	26.2%	$\pi^+\pi^-2\pi^0$	11.0%
$2\pi^+\pi^-2\pi^0$	42.8%	$\pi^+\pi^-3\pi^0$	28.0%
$2\pi^+\pi^-2\omega$	0.003%	$2\pi^+2\pi^-$	7.1%
$3\pi^+2\pi^-\pi^0$	8.4%	$2\pi^+2\pi^-\pi^0$	24.0%
		$\pi^+\pi^-\omega$	10.0%
		$2\pi^+2\pi^-2\pi^0$	10.0%

Because of abundant cosmogenic activity, each 2.3 ms event includes multiple reconstructed cosmic candidate interactions in the LAr volume, referred to as “clusters”. Three-dimensional clusters are reconstructed using the WireCell reconstruction package [37] as collections of 3D spacepoints, where each spacepoint carries information about its corresponding wire position, time-tick, and charge deposition. The true $n \to \bar{n}$ interaction clusters are identifiable through the comparison of two events (one with and one without a signal interaction) with the same background overlay source, as depicted in Fig. 1. The topological features of the signal clusters (“star-like”) and the background clusters (“straight track-like”) are then used to develop the selection as described in the next section.

IV. ANALYSIS TECHNIQUES AND SELECTION CRITERIA

The cluster reconstruction is followed by a series of selection criteria which are applied in three stages. The first, or preselection, stage makes use of a Boosted Decision Tree (BDT) using xgboost [38] to significantly reduce the number of background clusters while maintaining high signal efficiency. The BDT is trained using variables that contain information about the number of spacepoints along with wire positions and time associated with the spacepoints of each cluster, and which are shown in Fig. 2. We define the “extent” of a cluster as the number of wires or time-ticks over which the cluster is contained in the U, V, or Y wire-plane or time-tick dimension (one time-tick corresponds to 0.5 μs), respectively. These variables enable us to distinguish between signal and background clusters based on their topological features, such as the more localized, spherical topology for the signal $n \to \bar{n}$ clusters and the straight, track-like topology for the background clusters.

The BDT training outcome exhibits a clear separation between the signal ($n \to \bar{n}$) and background (cosmic) processes, as shown in Fig. 3 (left). Selecting clusters with BDT score > 0.1 rejects 91% of the background clusters and maintains high signal efficiency of 86%.

The second stage of selection applies an image-based selection criterion, using a sparse CNN with the VGG16 network architecture [22, 23, 39, 40]. A sparse CNN makes use of localized inputs within an image (star-like topology for the signal clusters and straight track-like topology for the background clusters) that highlight features on which the network trains rather than the full image. This selection stage makes use of 2D projections of the preselected clusters onto three sense wire planes of the MicroBooNE detector. These projections contain information about the wire position, time-tick, and charge deposition associated with each cluster, and are formatted in such a way so as to retain only the pixels associated with the signal or background clusters, thus making it highly memory efficient. The trained CNN’s performance on the test sample is shown in Fig. 3 (right).

The CNN score criterion is optimized with respect to the projected sensitivity at 90% CL. As a prerequisite for the sensitivity calculation, efficiencies for the signal and background events are calculated for various CNN score criteria and are shown in Table II. For these particular CNN score criteria (where the background rejection is $\sim 99\%$), preliminary sensitivity values were calculated, using the TRolke package in ROOT [41], based on the following assumptions:

- The assumed search region statistics correspond to 372 s of exposure, and were evaluated by scaling the test sample (containing $\times 10$ higher statistics) by a factor of 0.1, making it equivalent in size to the MicroBooNE “data” statistics for the analysis.
- The statistical uncertainty on the background is considered within the TRolke method, assuming Gaussian fluctuations on the data-sized test. The sensitivity calculation within TRolke assumes zero signal and hence no statistical uncertainty is assumed on the signal.
- The systematic uncertainty on the signal selection efficiency, for the CNN score criterion optimization study, is approximated to be 15% uncertainty. The systematic uncertainty on the background is evaluated as the statistical uncertainty on the background obtained using the test sample, as the background is measured in-situ.

Considering sensitivity as a figure of merit, the optimal CNN criterion is found to be 0.80.

After CNN selection, approximately 2% of the remaining clusters have zero extent in time or one of the wire dimensions, as a consequence of reconstruction inefficiencies [42]. Therefore, a third and final selection stage, based on topological information, is applied to reject zero- and low-extent clusters, which cannot represent the signal topology. The distributions of

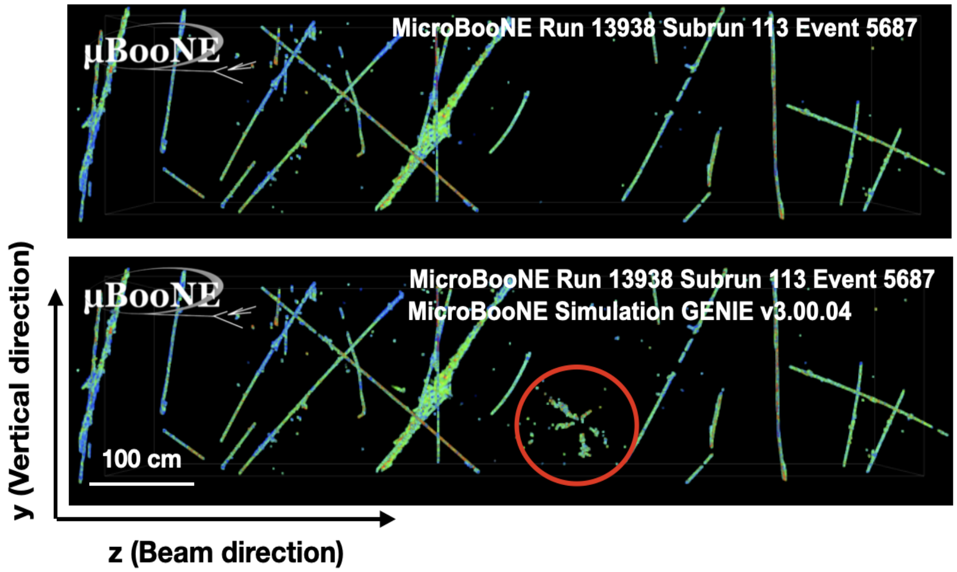

FIG. 1. (top) Event display showing an event with background clusters, collected in MicroBooNE off-beam data. (bottom) Event display showing an event with a GENIE-simulated $n-\bar{n}$ signal cluster (highlighted in the red circle) overlaid on top of the same background event. The vertical and horizontal scales are the same. Color represents the amount of deposited ionization charge where dark blue corresponds to 1/3 the energy deposited by a Minimum Ionizing Particle (MIP). Similarly, cyan, green, and red correspond to energy deposited by 1 MIP, 2 MIP and 4 MIP respectively.

TABLE II. Preliminary sensitivity for various CNN score criteria around the optimized score of 0.80. The signal and background efficiencies are calculated using the test sample. The background is also estimated using the test sample and then scaled by a factor of 0.1 to make it equivalent in size to the MicroBooNE data sample which corresponds to 372 s of exposure. Errors in the table account for finite MC statistics only.

CNN criterion	Signal Efficiency	Background Efficiency(10^{-4})	Background Estimate	Sensitivity (10^{25} yrs)
0.797	0.8274 ± 0.0003	1.53 ± 0.10	24.8 ± 1.6	2.62
0.798	0.8222 ± 0.0003	1.27 ± 0.09	20.5 ± 1.4	2.83
0.799	0.8012 ± 0.0003	1.08 ± 0.08	17.5 ± 1.3	2.98
0.800	0.7360 ± 0.0003	0.88 ± 0.07	14.2 ± 1.2	2.99
0.801	0.6392 ± 0.0004	0.66 ± 0.06	10.7 ± 1.0	2.95
0.802	0.5081 ± 0.0004	0.50 ± 0.06	8.1 ± 0.9	2.65
0.803	0.3490 ± 0.0004	0.43 ± 0.05	6.9 ± 0.8	1.95

extent variables after CNN selection are shown in Fig. 4 and the final selection criteria are chosen by visual inspection of these variables. The final selection requires the extent of a cluster in at least one of the three wire dimensions to be >70 wires, and in the time dimension to be >70 time-ticks. The final selection criteria were chosen to effectively reject the majority of background events, particularly those peaking in the range between 0 and 70 in extent as shown in Fig. 4.

The number of signal and background events in the test sample before and after each of the three selection stages is shown in Table III. The analysis yields an overall signal selection efficiency of 70.0%, corresponding to the ratio of events at stage 3 to events before any selection. At the same time, it rejects 99.99% of the total background.

TABLE III. The number of predicted signal and background events in the test sample before and after each of the three selection stages.

Selection Stage	Signal	Background
No selection	1,633,525	1,618,827
Stage 1	1,411,164	139,802
Stage 2	1,202,281	142
Stage 3	1,147,157	32
Signal selection efficiency	70.0%	-
Background rejection efficiency	-	99.99%

V. SYSTEMATIC UNCERTAINTIES

The systematic uncertainties on signal and background events are assessed independently. Systematic uncertain-

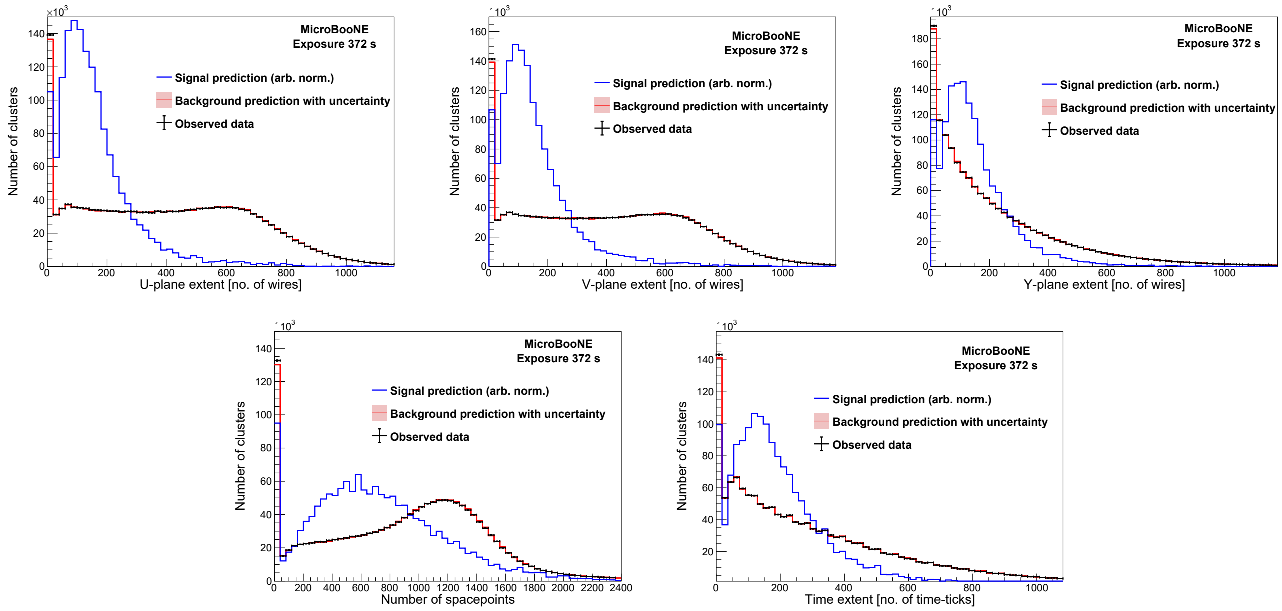

FIG. 2. Distributions of topological variables from 2D cluster projections for the signal (blue) and background (red) clusters. The background is shown along with its systematic uncertainty band. The systematic uncertainty is small and of the order of a few percent. The data points corresponding to 372 s of exposure are shown (after unblinding) in black along with statistical uncertainty. The background clusters, generated with a test sample, are normalized exactly to match the data exposure of 372 s, whereas the signal clusters, which were simulated and overlaid onto the background clusters, were arbitrarily normalized as they can not be precisely scaled to match the data exposure. The samples used to obtain background prediction and data are assumed to have a negligible signal.

ties on the signal selection efficiency include contributions from GENIE, Geant4, and detector model variations.

A. GENIE Systematics

The default GENIE model used in MicroBooNE to simulate $n-\bar{n}$ interactions is the hA-Local Fermi Gas (hA-LFG) model. The signal efficiency using simulations with other possible model variations has been evaluated. GENIE offers various models to describe the energy and momentum of the initial state nucleon, such as Bodek-Ritchie (BR) or Local Fermi Gas (LFG). Similarly, final state interactions (FSI) are described in GENIE either through a full cascade model (hN) or an effective model that parameterizes FSI as a single interaction (hA). For each variation, a new independent signal sample is generated, and the entire selection, as described in Sec. IV, is applied to each of them to evaluate signal selection efficiency, and subsequently, the associated uncertainty. Table IV shows the quantitative estimate of uncertainty due to various GENIE models on signal selection efficiency. The fractional uncertainty on the signal selection efficiency, η, is the uncertainty on the efficiency for each model (ϵ) with respect to the nominal GENIE hA-LFG model (ϵ_{nom}) calculated using Eq. 3. This equation does not consider statistical uncertainty on the efficiency evaluated for each model which is found to be negligible (2×10^{-4}).

TABLE IV. The fractional uncertainty in signal efficiency η is shown for various samples with different GENIE models. The total uncertainty due to GENIE modeling, obtained by taking the squared sum of η, is estimated to be 4.85%.

GENIE model	η (%)
hA-BR	1.17
hN-BR	4.56
hN-LFG	1.14
Total	4.85

$$\eta = \frac{\epsilon_{nom} - \epsilon}{\epsilon_{nom}} \tag{3}$$

The total fractional uncertainty on the signal efficiency due to GENIE systematic uncertainties is estimated to be 4.85%.

B. Geant4 Systematics

Uncertainty from Geant4 accounts for hadron-^{40}Ar re-interaction uncertainties. Charged hadrons can interact

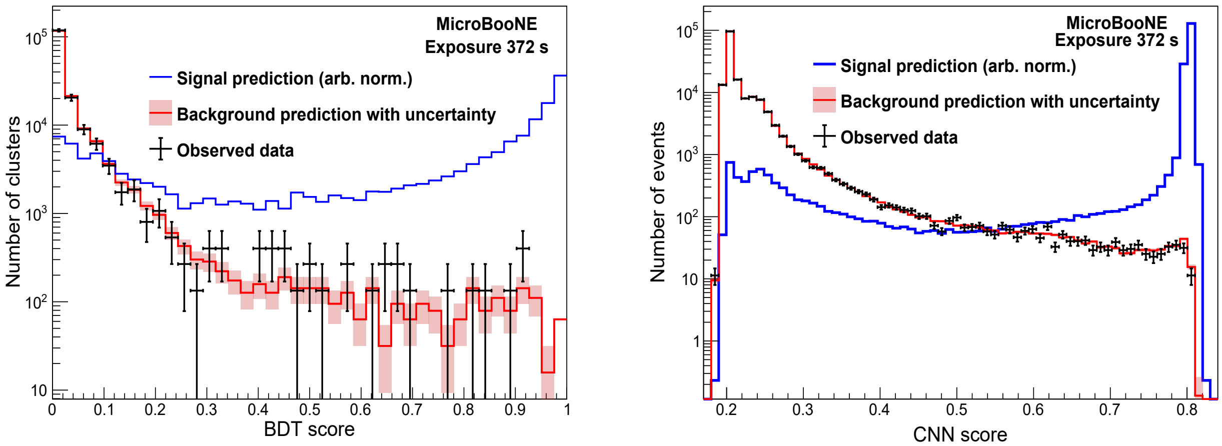

FIG. 3. Classification performance of the BDT (left) and CNN (right) for the signal $n \to \bar{n}$ (blue) and background (red) clusters. The background is shown along with the systematic uncertainty band. The data points corresponding to 372 s of exposure are shown (after unblinding) in black along with statistical uncertainty. The background clusters, generated with a test sample, are normalized exactly to match the data exposure of 372 s, whereas the signal clusters, which were simulated and overlaid onto the background clusters, were arbitrarily normalized as they can not be precisely scaled to match the data exposure. The samples used to obtain background prediction and data are assumed to have a negligible signal.

with external ^{40}Ar nuclei while traveling through the liquid argon volume. Inelastic re-interactions of hadrons (π^+, π^-, p) in the LAr volume are simulated by Geant4, and the cross-sections of these hadronic re-interactions are varied to account for the corresponding systematic uncertainty. The uncertainty of these scattering processes of protons and charged pions can be significant, especially when there are many charged hadrons in the final state, such as in $n \to \bar{n}$ interactions. The impact of hadron re-interaction uncertainty on $n \to \bar{n}$ signal efficiency has been evaluated using an event re-weighting scheme [43]. The systematic uncertainty (σ) due to hadron (π^+, π^-, p) re-interactions is assessed using the following equation for each hadron

$$\sigma = \frac{1}{N_{\rm w}} \sum_{i=1}^{N_{\rm w}} (W_{\rm i} - N)^2, \tag{4}$$

where i runs over the number of re-weights ($N_{\rm w}$=1000) generated for each of the π^+, π^- and proton, re-interactions. Table V shows the fractional uncertainty on the signal efficiency due to hadron re-interaction uncertainties with a total Geant4 uncertainty evaluated to be 2.32%.

TABLE V. The fractional uncertainty in signal efficiency σ is shown for various samples with different Geant4 re-interaction weights in last column. The total uncertainty due to Geant4 modeling, obtained by taking the squared sum of σ, is estimated to be 2.32%.

Geant4 re-interactions	σ (%)
π^+	0.89
π^-	1.3
proton	1.7
Total	2.32

C. Detector Systematics

The detector modeling and response uncertainties are evaluated for the signal sample using a novel data-driven technique [44] to account for discrepancies between data and simulation in charge and light response. This uses *in-situ* measurements of distortions in the TPC wire readout signals due to various detector effects, such as diffusion, electron drift lifetime, electric field, and electronics response, to parametrize these effects at the TPC wire level.

For each variation, a new independent signal MC sample is generated. The final selection is applied to each of these samples and signal efficiency is calculated. Table VI shows the fractional uncertainty due to various detector variations on the signal selection efficiency. The fractional uncertainty on signal selection efficiency (quoted in the last column) includes a statistical uncertainty in efficiency η_{err} and uncertainty in efficiency due to each detector variation with respect to the nominal η_{errnom} which are defined as

$$\eta_{\rm err} = \sqrt{\frac{\epsilon(1-\epsilon)}{N}}, \tag{5}$$

where ϵ and N are the signal efficiency and the number of

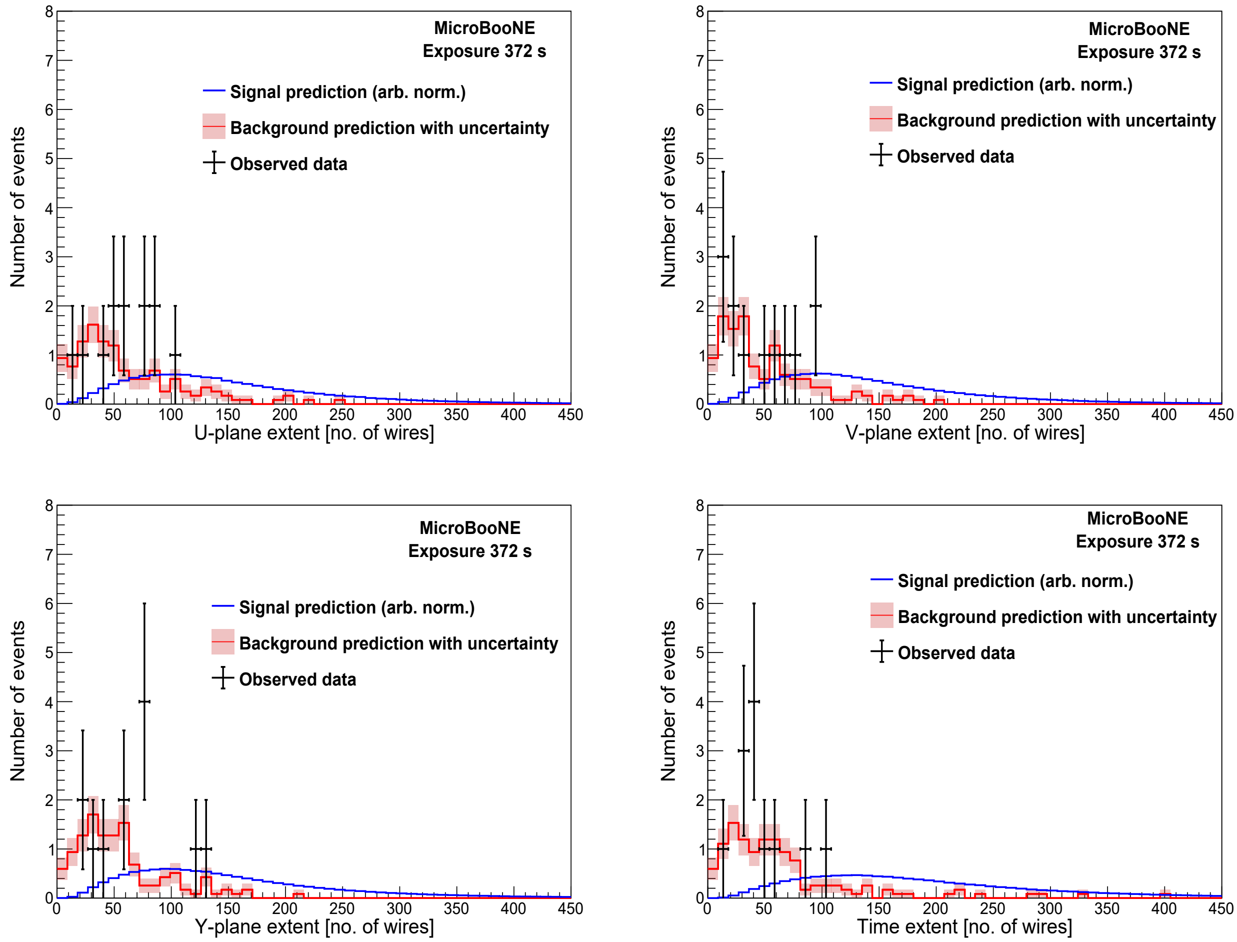

FIG. 4. The distributions of U,V,Y-plane and time-tick extents for the signal $n \to \bar{n}$ (blue) and background (red) events are shown. The data points corresponding to 372 s of exposure are shown (after unblinding) in black along with statistical uncertainty. The background events, generated with a test sample, are normalized exactly to match the data exposure of 372 s, whereas the signal events, for which the clusters were simulated and overlaid onto the background clusters, were arbitrarily normalized as they can not be precisely scaled to match the data exposure. The samples used to obtain background prediction and data are assumed to have a negligible signal.

generated events, respectively, for any given model, and

$$\eta_{errnom} = \frac{\epsilon_{nom} - \epsilon}{\epsilon_{nom}}, \tag{6}$$

where ϵ_{nom} represents the signal efficiency with the nominal sample. The total fractional uncertainty due to detector modeling is evaluated to be 6.72%.

The total fractional uncertainty on the signal selection efficiency when treating GENIE, Geant4, and detector systematics as being uncorrelated, is 8.61%. The systematic uncertainty on the background is 17.68%, and it corresponds to the statistical uncertainty on the number of final selected background events in the test sample shown in Table III.

VI. SENSITIVITY EVALUATION

The final event selection, as described in Sec. IV, yields an expected background of $(3.2 \pm 0.56(\text{stat}) \pm 0.17(\text{syst}))$ events corresponding to 372 s of exposure, obtained by normalizing the background events reported in Table III by a factor of 0.1 to predict the background from the data-sized sample. The sensitivity to the ^{40}Ar-bound $n \to \bar{n}$ lifetime is evaluated using the TRolke statistical method [41] following a frequentist approach. This method takes into account both statistical and systematic uncertainties along with various statistical models to account for signal selection efficiency and background contamination. We use a Gaussian model that describes the expectation along with a standard deviation for both the background and signal selection efficiency. The sensitivity is evaluated assuming the absence of any signal

TABLE VI. The percent uncertainty in signal efficiency η is shown for various samples with different detector systematic variations in the last column. The total uncertainty due to detector systematics, obtained by taking the squared sum of the last column, is estimated to be 6.73%.

Detector variation	η_{err} %	η_{errNom} %	η %
Recombination	0.13	0.53	0.54
Light yield	0.22	1.15	1.17
Space charge effect	0.12	0.13	0.18
TPC waveform modeling	0.24	6.59	6.59
Total			6.72

contribution, treating any observed events as indistinguishable from the background events. The resulting τ_m sensitivity for ^{40}Ar corresponds to 6.0×10^{25} years at 90% CL.

VII. FAKE-DATA ANALYSIS

The analysis is developed as a blind analysis and the final selection is tested on a dedicated fake-data sample before looking at the data sample reserved for making the final measurement. The fake-data sample corresponds to a data-sized sample of unbiased, off-beam data events (372 s of exposure), which is statistically independent from the data sample and is prepared with a blinded fraction of x% injected $n{-}\bar{n}$ signal, where x% is unknown to the analyzer. As part of the fake-data test, the x% is estimated from the developed analysis framework by performing a fit to the fake data. The final selection, as described in Sec. IV, is applied to the fake-data sample. Out of 158,681 events, 268 events passed the selection, with an expected background of 3.2.

Next, the compatibility of the fake-data observation with the expectation was quantized by constructing a χ^2 as follows:

$$\chi^2 = \frac{(O-E)^2}{E}, \tag{7}$$

where $O = 268$ is the observed number of events in the fake-data sample, and E is the expected background plus $n \to \bar{n}$ signal events and is defined as

$$E = x_{\rm fit} N_{\rm g} \epsilon_{\rm s} + (1 - x_{\rm fit}) N_{\rm g} \epsilon_{\rm b} \tag{8}$$

where $x_{\rm fit}$ is the assumed fraction of injected $n \to \bar{n}$ events in the fake-data sample, $N_{\rm g} = 158,681$ is the number of events in the fake-data sample, $\epsilon_{\rm s} = 0.70$ is the signal selection efficiency, and $\epsilon_{\rm b} = 1.97 \times 10^{-5}$ is the background efficiency. x_{fit} is varied to obtain the minimum χ^2 value, corresponding to the best-fit x_{bf}. Figure 5 shows the expected number of events and χ^2 distribution as a function of $x_{\rm fit}$. The best-fit fraction of $n \to \bar{n}$ signal is found to be 0.23%, whereas the actual fraction revealed after this measurement was performed is 0.25%. The estimated fraction matches the actual fraction within the 1σ uncertainty of 0.03% demonstrating the validity of this analysis.

VIII. RESULTS

After successfully validating the developed analysis selection using the fake-data sample, the analysis examined the data sample reserved for reporting the final measurement, corresponding to 372 s of exposure. Upon applying the analysis selection criteria, 2 events are observed, with an expected background of (3.2 ± 0.56(stat)± 0.17(syst)) events. The observed events are shown in Fig. 6.

The lack of excess of events above the expected background prediction leads to a demonstrative lower bound on the ^{40}Ar-bound $n \to \bar{n}$ lifetime of 1.1×10^{26} years at 90% CL. Using Eq.(1) and $R = 5.6 \times 10^{22}$ s^{-1} for ^{40}Ar [19], a limit on the free-neutron equivalent $n \to \bar{n}$ lifetime is derived as $\tau_{\rm n-\bar{n}} > 2.6 \times 10^5$ s. This also is subject to an additional uncertainty associated with R, which is estimated at 15% [19].

IX. CONCLUSIONS

We have developed and validated a novel approach to search for neutron-antineutron transitions in ^{40}Ar using the MicroBooNE detector. This methodology, based on state-of-the-art reconstruction tools and deep learning methods specifically tailored for LArTPC experiments, showcases the high sensitivity capabilities of LArTPCs in this search. As a proof-of-principle demonstration, we make use of the off-beam data from the MicroBooNE detector under the assumption that this data contains negligible signal events, consistently with Super-K results [4], to provide a lower limit on the mean neutron-antineutron transition time that is far lower compared to those of previous measurements, due to limited exposure and non-competitive detector mass. The selection achieves a uniquely high signal selection efficiency of 70.0% and a background rejection efficiency of 99.99%; the former of these represents a large improvement over previous results, which reported 4.1% signal efficiency [4]. With an already well-developed methodology, this study demonstrates the future potential of enhanced sensitivities within forthcoming LArTPC-based detectors such as DUNE in their searches for such rare signals; further improvements, such as delineating the actual kinematics of signals and backgrounds, show still more promise. It is important to note that the backgrounds in DUNE

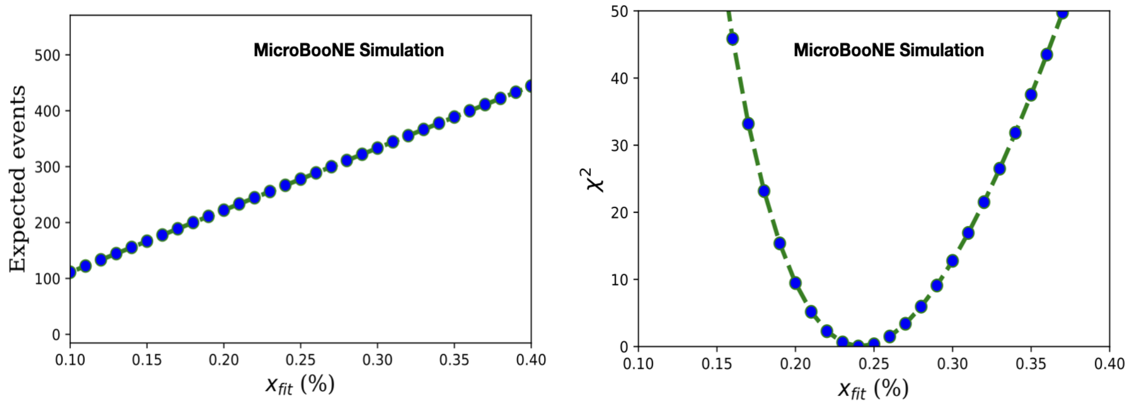

FIG. 5. Distributions of expected events (left) and χ^2 (right) of fake-data observation are shown as a function of the fraction of injected $n \to \bar{n}$ events in fake-data sample, x_{fit}.

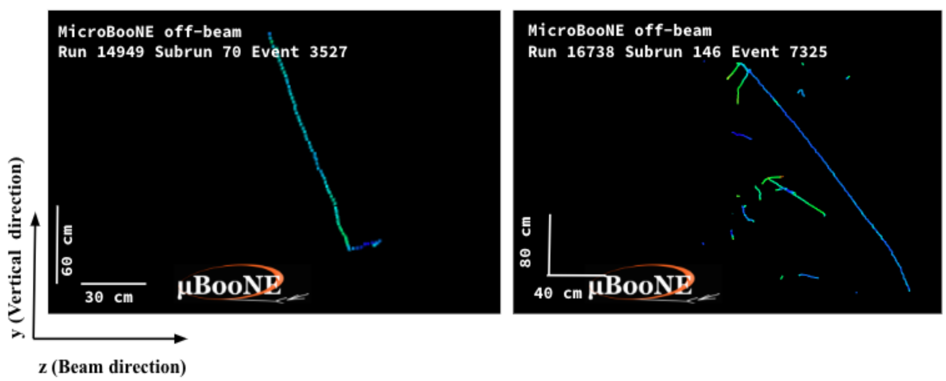

FIG. 6. Event displays of the two data events that pass final analysis selection. Only the selected cluster from the final selection is shown for both events. The x-axis represents the beam direction and the y-axis represents the vertical direction. Color represents the amount of deposited charge where dark blue corresponds to 1/3 the energy deposited by a Minimum Ionizing Particle (MIP). Similarly, cyan, green, and red correspond to energy deposited by 1 MIP, 2 MIP and 4 MIP respectively.

and MicroBooNE are distinct. While cosmic ray muons are the dominant backgrounds in MicroBooNE, atmospheric neutrino interactions are expected to be the main source of backgrounds in DUNE. Nonetheless, the presented analysis demonstrates the usefulness of machine learning techniques and of particularly simple topological extent variables only available to LArTPCs, confirming the capabilities of larger, well-shielded LArTPCs such as DUNE to perform high-sensitivity searches for baryon number violation.

ACKNOWLEDGMENTS

This document was prepared by the MicroBooNE collaboration using the resources of the Fermi National Accelerator Laboratory (Fermilab), a U.S. Department of Energy, Office of Science, HEP User Facility. Fermilab is managed by Fermi Research Alliance, LLC (FRA), acting under Contract No. DE-AC02-07CH11359. MicroBooNE is supported by the following: the U.S. Department of Energy, Office of Science, Offices of High Energy Physics and Nuclear Physics; the U.S. National Science Foundation; the Swiss National Science Foundation; the Science and Technology Facilities Council (STFC), part of the United Kingdom Research and Innovation; the Royal Society (United Kingdom); the UK Research and Innovation (UKRI) Future Leaders Fellowship; and the NSF AI Institute for Artificial Intelligence and Fundamental Interactions. Additional support for the laser calibration system and cosmic ray tagger was provided by the Albert Einstein Center for Fundamental Physics, Bern, Switzerland. We also acknowledge the contributions of technical and scientific staff to the design, construction, and operation of the MicroBooNE detector as well as the contributions of past collaborators to the development of MicroBooNE analyses, without whom this work would not have been possible. We gratefully acknowledge W. J. Willis for his leadership on the MicroBooNE experiment and formative contributions to $n \to \bar{n}$ searches with LArTPCs. For the purpose of open access, the authors have applied a Creative Commons Attribu-

tion (CC BY) public copyright license to any Author Accepted Manuscript version arising from this submission.

[1] K. S. Babu, P. S. Bhupal Dev, E. C. F. S. Fortes, and R. N. Mohapatra, Phys. Rev. D **87**, 115019 (2013), arXiv:1303.6918 [hep-ph].
[2] M. Fukugita and T. Yanagida, Phys. Lett. B **174**, 45 (1986).
[3] J. M. Arnold, B. Fornal, and M. B. Wise, Phys. Rev. D **87**, 075004 (2013), arXiv:1212.4556 [hep-ph].
[4] K. Abe *et al.* (Super-Kamiokande Collaboration), Phys. Rev. D **103**, 012008 (2021).
[5] E. S. Golubeva, J. L. Barrow, and C. G. Ladd, Phys. Rev. D **99**, 035002 (2019), arXiv:1804.10270 [hep-ex].
[6] E. Klempt, C. Batty, and J.-M. Richard, Physics Reports **413**, 197 (2005).
[7] C. Amsler *et al.* (Crystal Barrel), Nucl. Phys. A **720**, 357 (2003).
[8] M. Baldo-Ceolin *et al.*, Z. Phys. C **63**, 409 (1994).
[9] M. L. Cherry, K. Lande, C. K. Lee, R. I. Steinberg, and B. Cleveland, Phys. Rev. Lett. **50**, 1354 (1983).
[10] T. W. Jones *et al.* (**IMB** Collaboration), Phys. Rev. Lett. **52**, 720 (1984).
[11] G. Fidecaro *et al.* (CERN-ILL-Padova-Rutherford-Sussex Collaboration), Phys. Lett. B **156**, 122 (1985).
[12] M. Takita *et al.* (Kamiokande Collaboration), Phys. Rev. D **34**, 902 (1986).
[13] G. Bressi *et al.*, Nuovo Cim. A **103**, 731 (1990).
[14] Ch. Berger *et al.* (Frejus Collaboration), Phys. Lett. B **240**, 237 (1990).
[15] K. Abe *et al.* (Super-Kamiokande), Phys. Rev. D **91**, 072006 (2015), arXiv:1109.4227 [hep-ex].
[16] M. Baldo-Ceolin *et al.*, Z. Phys. C **63**, 409 (1994).
[17] J. Chung *et al.*, Phys. Rev. D **66**, 032004 (2002), arXiv:hep-ex/0205093.
[18] B. Aharmim *et al.* (SNO), Phys. Rev. D **96**, 092005 (2017), arXiv:1705.00696 [hep-ex].
[19] J. L. Barrow, E. S. Golubeva, E. Paryev, and J.-M. Richard, Phys. Rev. D **101**, 036008 (2020), arXiv:1906.02833 [hep-ex].
[20] E. Friedman and A. Gal, Phys. Rev. D **78**, 016002 (2008).
[21] J. L. Barrow, A. S. Botvina, E. S. Golubeva, and J. M. Richard, Phys. Rev. C **105**, 065501 (2022), arXiv:2111.10478 [hep-ex].
[22] B. Graham, M. Engelcke, and L. van der Maaten, CoRR **abs/1711.10275** (2017), 1711.10275.
[23] B. Graham and L. van der Maaten, CoRR **abs/1706.01307** (2017), 1706.01307.
[24] B. Abi *et al.* (DUNE Collaboration), Eur. Phys. J. C **80**, 978 (2020), arXiv:2006.16043 [hep-ex].
[25] B. Abi *et al.* (DUNE Collaboration), Eur. Phys. J. C **81**, 322 (2021), arXiv:2008.12769 [hep-ex].
[26] B. Abi *et al.* (DUNE Collaboration), Eur. Phys. J. C **81**, 423 (2021), arXiv:2008.06647 [hep-ex].
[27] R. Acciarri *et al.* (MicroBooNE Collaboration), J. Instrum. **12**, P02017 (2017).
[28] P. Abratenko *et al.* (MicroBooNE Collaboration), (2023), arXiv:2304.02076 [hep-ex].
[29] C. Andreopoulos *et al.*, Nucl. Instrum. Meth. A **614**, 87 (2010).
[30] C. Andreopoulos *et al.*, arXiv (2015), 1510.05494 [hep-ph].
[31] J. E. T. Hewes, *Searches for Bound Neutron-Antineutron Oscillation in Liquid Argon Time Projection Chambers*, Ph.D. thesis, Manchester U. (2017).
[32] R. D. Woods and D. S. Saxon, Phys. Rev. **95**, 577 (1954).
[33] S. Agostinelli *et al.* (GEANT4), Nucl. Instrum. Meth. A **506**, 250 (2003).
[34] E. Snider and G. Petrillo, J. Phys. Conf. Ser. **898**, 042057 (2017).
[35] R. Pordes and E. Snider, PoS **ICHEP2016**, 182 (2016).
[36] D. H. Wright and M. H. Kelsey, Nucl. Instrum. Meth. A **804**, 175 (2015).
[37] P. Abratenko *et al.* (MicroBooNE), JINST **16**, P06043 (2021), arXiv:2011.01375 [physics.ins-det].
[38] T. Chen and C. Guestrin, Proceedings of the 22nd ACM SIGKDD International Conference on Knowledge Discovery and Data Mining (2016), 10.1145/2939672.2939785.
[39] P. Abratenko *et al.* (MicroBooNE Collaboration), Phys. Rev. D **103**, 052012 (2021).
[40] P. Abratenko *et al.* (MicroBooNE Collaboration), JINST **17**, P09015 (2022), arXiv:2201.05705 [hep-ex].
[41] W. A. Rolke and A. M. Lopez, Nucl. Instrum. Meth. A **458**, 745 (2001), arXiv:hep-ph/0005187.
[42] P. Abratenko *et al.* (MicroBooNE Collaboration), Phys. Rev. Lett. **128**, 151801 (2022).
[43] J. Calcutt, C. Thorpe, K. Mahn, and L. Fields, JINST **16**, P08042 (2021).
[44] P. Abratenko *et al.* (MicroBooNE Collaboration), Eur. Phys. J. C **82**, 454 (2022), arXiv:2111.03556 [hep-ex].